Interactions between tidal stream turbine arrays and their hydrodynamic impact around Zhoushan Island, China

Interactions between tidal stream turbine arrays and their hydrodynamic impact around Zhoushan Island, China

Jisheng Zhang[a,d], Can Zhang[a,b,d,*], Athanasios Angeloudis[c], Stephan C. Kramer[b], Rui He[a,d] and Matthew D. Piggott[b,*]

[a]Key Laboratory of Ministry of Education for Coastal Disaster and Protection , Hohai University, Nanjing 210024, China
[b]Department of Earth Science and Engineering, Imperial College London, London, SW7 2AZ, UK
[c]School of Engineering, Institute for Infrastructure and the Environment, The University of Edinburgh, Edinburgh, EH8 9JU, UK
[d]College of Harbor, Coastal and Offshore Engineering, Hohai University, Nanjing, 210098, China

ARTICLE INFO

Keywords:
Tidal stream energy
Multi-arrays
Optimisation
Competition effect
Hydrodynamic impact

ABSTRACT

Tidal currents represent an attractive renewable energy source particularly because of their predictability. Prospective tidal stream development sites are often co-located in close proximity. Under such circumstances, in order to maximise the exploitation of the resource, multiple tidal stream turbine arrays working in tandem would be needed. In this paper, a continuous array optimisation approach based on the open source coastal ocean modelling framework *Thetis* is applied to derive optimal configurations for four turbine arrays around Zhoushan Islands, Zhejiang Province, China. Alternative optimisation scenarios are tested to investigate interactions between the turbine arrays and their hydrodynamic footprint. Results show that there are no obvious competition effects between these four arrays around Hulu and Taohua Island. However, significant interactions could arise among the three turbine arrays situated around Hulu Island, with a maximum decrease in average power of 42.2%. By optimising all turbine arrays simultaneously, the competition effects can be minimised and the cost of energy reduced as less turbines are required to deliver an equivalent energy output. As for the potential environmental impact, it is found that the turbine array around Taohua Island would affect a larger area than turbine arrays around Hulu Island.

1. Introduction

Tidal stream energy represents a promising alternative renewable energy source that could offset the use of fossil fuels in the future (Zheng and Zhang, 2015). Since it is predictable (as opposed to wind, solar and other renewable energy sources), sustainable and relatively friendly to the environment, much attention has been paid to tidal stream energy. In particular, a key focus has been the evaluation of the resource at local and regional scales, and the determination of appropriate means to harness this resource effectively. Many countries have rich tidal stream energy resource (Hammons, 2008; Grabbe et al., 2009; Defne et al., 2012; Kim et al., 2012; Moore and Boyle, 2014). In China, the resource is estimated at 13.95 GW, half of which is contained in the waters of Zhejiang province (Wang et al., 2011). The area around Zhoushan Islands, within Zhejiang province, has the highest potential tidal stream energy resource. The maximum tidal stream velocity in the channel between Hulu Island and Putuoshan Island is above 1.7 m/s and the water depth varies from 20 m to 60 m (Wang et al., 2010). Therefore, the first tidal stream energy demonstration project with a turbine testing function in China is located there. In this paper, the deployment of multiple nearby tidal stream turbine arrays in this area are considered to explore potential competition effects between them as well as their influence on the wider hydrodynamic environment.

Tidal stream turbines have been studied extensively both physically and numerically (Chen, 2015; Zhang et al., 2020b). A typical result based upon investigation of a single turbine in a simple idealised channel is that the flow velocity would recover to approximately 80% of its free stream value within a distance of $20D$ (where D is the diameter of the turbine) downstream of the turbine. The percentage comes close to 100% within $40D$ downstream of the turbine (Zhang et al., 2017, 2020c). It should be noted that these values will be strongly affected by real world flow structures including ambient turbulence levels. Nevertheless, these empirical results allow for generic array design guidelines to be drawn up based upon ideal conditions.

However, in realistic applications turbine arrays in the future are likely to contain dozens if not hundreds of individual devices, which leads to a far more complex engineering design challenge. As such, optimising a tidal stream turbine array's configuration in order to extract tidal stream energy as efficiently as possible remains an active research topic. When turbines are deployed in a staggered manner, previous work has found a $5D$ row-spacing to be a sensible approach (O'Doherty et al., 2011; Fallon et al., 2014). The appropriate lateral distance between turbines in the same row has previously been identified to be in the order of $2.5D$ (Bai et al., 2013). However, these approaches do not take account of local flow variations which will mean that the optimal design will be more complex than what can be defined through uniform inter- and intra-row spacing values. Alternatively, Funke et al. (2014) proposed a more flexible gradient-based optimisation method which improves the

*Corresponding author
z.can19@imperial.ac.uk (.C. Zhang); m.d.piggott@imperial.ac.uk (.M.D. Piggott)
ORCID(s): 0000-0002-0041-038X (.C. Zhang)

micro-siting of individual turbines within an array in an arbitrary manner, with only bound constraints on the locations turbines can occupy (e.g. the lease area) and a minimum turbine spacing. This leads to an unstructured, non-simply-staggered, layout which is able to yield more efficient performance. This approach has already been used to design a turbine array around Zhoushan Island and notable improvement was achieved in terms of the energy yield (Wang et al., 2017; Zhang et al., 2020a).

While a larger number of turbines in an array can, up to a point, increase yield, it will generally also lead to a more significant impact on the hydro-environment. Tidal elevation may increase upstream of the turbine array, and decrease downstream leading to the formation of a hydraulic gradient driving the flow (De Dominicis et al., 2017). Tidal velocities are also generally reduced overall within the array through energy extraction and dissipation as the flow interacts with turbines. Meanwhile, velocity magnitude can be increased at the sides of the array as bypassing flow is redirected towards areas of lower resistance (Chen et al., 2013). In addition, the environmental impact of energy extraction is not necessarily restricted to the immediate vicinity of the turbine array, and a far-field area may also be impacted (Ahmadian et al., 2012; Martin-Short et al., 2015; du Feu et al., 2017, 2019).

Although the above studies have considered the challenge of improving an array's performance and investigated their impact, fewer consider multiple nearby but distinct arrays which would become common with the development of the tidal stream energy industry. Assuming that arrays are not designed simultaneously, then negative interactions may influence an array's performance and this potential impact should be explored. In addition, cumulative impacts on the environment may scale nonlinearly and add complexity as the number of arrays developed increases. Funke et al. (2016) developed and applied a gradient-based approach to optimise four arrays in the Pentland Firth, both individually and simultaneously. The result showed that there can be a clear difference between these two optimisation strategies. More recently, Goss et al. (2018, 2020) applied a similar approach using the *Thetis* model to the Alderney Race region and studied the competition effects between two directly adjacent turbine arrays.

In this paper *Thetis* is used to simulate the tidal flow around Zhoushan Islands, China under realistic conditions. Compared to the *OpenTidalFarm (OTF)* model used in previous studies (Funke et al., 2014, 2016; Zhang et al., 2020a), *Thetis* uses an improved discretisation method (Kärnä et al., 2018) to model the tidal dynamics, but uses the same adjoint-based optimisation strategy as in (Funke et al., 2016). Specifically, when solving the governing partial differential equations (PDEs), *Thetis* uses a discontinuous Galerkin based method for the spatial discretisation while OTF uses a continuous method, which leads to improvements in the accuracy of the hydrodynamic simulation. Four turbine arrays, one around Taohua Island and three around Hulu Island, are optimised under different optimisation scenarios to maximise the total energy output. The interaction effects between these turbine arrays are studied and the hydrodynamic impacts are analysed. This study thus provides insight and guidance for the development of tidal stream energy generation in the Zhoushan Islands region subject to the objective of maximising total energy output.

2. Numerical Model

2.1. Hydrodynamic Model

The tidal flow around Zhoushan Islands is simulated using *Thetis* (`https://thetisproject.org/`), an open source coastal ocean modelling framework. *Thetis* is implemented using the *Firedrake* (`https://firedrakeproject.org/`) framework which is a code generation system for the solution of PDEs using the finite element method (FEM). *Thetis* has previously been applied to a number of tidal hydrodynamics applications, including the assessment of tidal energy schemes (Angeloudis et al., 2018; Harcourt et al., 2019; Angeloudis et al., 2020; Goss et al., 2020) and their hydro-environmental impacts (Vouriot et al., 2019; Baker et al., 2020). In this study, the elevation and velocity fields comprising the hydrodynamics are obtained by solving the nonlinear shallow water equations in their non-conservative form:

$$\begin{gathered}\frac{\partial \eta}{\partial t} + \nabla \cdot (H\boldsymbol{u}) = 0, \\ \frac{\partial \boldsymbol{u}}{\partial t} + \boldsymbol{u} \cdot \nabla \boldsymbol{u} - \nu \nabla^2 \boldsymbol{u} + f\boldsymbol{u}^{\perp} + g\nabla\eta = -\frac{\tau_b}{\rho H} - \frac{c_t}{\rho H} \|\boldsymbol{u}\| \boldsymbol{u},\end{gathered} \tag{1}$$

where η is the free surface displacement, and t is time. H is the total water depth, $\boldsymbol{u}$ is the depth-averaged velocity vector and ν is the kinematic viscosity of water. $f = f_0 + \beta y$ is the Coriolis frequency (Goss et al., 2018), with $f_0 = 2\omega \sin(\zeta)$ and $\beta = \frac{1}{R} 2\omega \cos(\zeta)$, where ω is the angular frequency of the Earth's rotation and ζ is the latitude which is set to the value at the middle of the domain. In turn, $\boldsymbol{u}^{\perp}$ is obtained by rotating the depth-averaged velocity through 90 degree counter clockwise. The variable τ_b is the natural bottom shear stress, which can be formulated via

$$\frac{\tau_b}{\rho} = g n^2 \frac{\|\boldsymbol{u}\| \boldsymbol{u}}{H_d^{\frac{1}{3}}}, \tag{2}$$

where g is the acceleration value due to gravity, n is the Manning coefficient which is typically determined based upon the bottom sediment size. Finally, c_t is an additional parameterisation used to represent the turbines' thrust and will be fully described in the following section.

2.2. Turbine Model

In the 2D non-linear shallow water model of *Thetis*, turbine arrays are parametrised as regions of enhanced bottom friction, with a spatially-varying non-dimensional bottom friction c_t (Funke et al., 2016; Goss et al., 2020). The force introduced by the presence of the turbine array in the model reads

$$\boldsymbol{F}_{array} = \int_{\Omega_{array}} \rho c_t(d(x)) \|\boldsymbol{u}\| \boldsymbol{u} \, dx, \tag{3}$$

where $d(x)$ is a function representing the spatially varying turbine density and the enhanced bottom friction c_t is a function of this field. The value of $d(x)$, and this c_t, is set to zero outside the area turbines are allowed to be deployed.

The thrust force of a collection of N turbines can be approximated as

$$\boldsymbol{F}_{array} = \sum_{i=1}^{N} \frac{1}{2}\rho C_t A_t \left\|\boldsymbol{u}_i\right\| \boldsymbol{u}_i, \tag{4}$$

where C_t is an individual turbine's thrust coefficient and A_T is the turbine's cross-sectional area, $\boldsymbol{u}_i$ is the free stream velocity at the i_{th} turbine's coordinates. Here, all turbines in an array are assumed to be identical so they have the same C_t and A_t. By replacing the summation in (4) by an integral, the continuous version can be defined as

$$\boldsymbol{F}_{array} = \int_{\Omega_{array}} \frac{1}{2}\rho C_t A_t d(x) \left\|\boldsymbol{u}(x)\right\| \boldsymbol{u}(x)\, dx. \tag{5}$$

By equating (3) with (5), an expression (Schwedes et al., 2017) for the enhanced bed friction c_t as a function of the turbine density $d(x)$ can be obtained

$$c_t(d(x)) = \frac{1}{2} C_T A_T d(x). \tag{6}$$

Then, given a turbine farm configuration described by a variable local turbine density field, $d(x)$, the instantaneous total energy output can be computed via

$$P(d, \boldsymbol{u}) = \boldsymbol{F}_{array} \cdot \boldsymbol{u} = \int_{\Omega} \rho c_t(d(x)) \left\|\boldsymbol{u}\right\|^3 \, dx, \tag{7}$$

with the average power generated over a tidal period computed using

$$P(d, \boldsymbol{u}) = \frac{1}{T} \int_0^T \int_{\Omega} \rho c_t(d(x)) \left\|\boldsymbol{u}\right\|^3 \, dx\, dt, \tag{8}$$

Note that in equating (3) and (5) we have assumed that the local velocity $\boldsymbol{u}(x)$, which in the model represents an average over the water column depth, and laterally between bypass and through-turbine flow, is a good representation of the free stream velocity of a turbine at that location. Similarly, for an accurate estimate of the power available to the turbine, we would have to use the, unknown, through-turbine velocity in $\boldsymbol{F} \cdot \boldsymbol{u}$. Instead we compute the total power extracted from the hydrodynamics through the turbine parameterisation, which includes unresolved mixing losses (see (Kramer and Piggott, 2016) for further discussion).

2.3. Optimisation Model

A gradient based optimisation algorithm is combined with the hydrodynamic solver in order to optimise array designs which are fully two-way coupled to the hydrodynamics. In other words, the task of finding optimal turbine array configurations is formulated as a PDE-constrained optimisation problem (Funke et al., 2014),

$$\begin{aligned} &\max_{\boldsymbol{u},\eta,d} \; J(\boldsymbol{u}, \eta, d), \\ &\text{subject to } F(\boldsymbol{u}, \eta, d) = 0, \\ &\qquad 0 \le d \le d_u, \end{aligned} \tag{9}$$

where $J(\boldsymbol{u}, \eta, d)$ is the functional of interest, $F(\boldsymbol{u}, \eta, d) = 0$ represents the non-linear shallow water equations, and d_u is an upper bound on the permitted turbine density. The overall optimisation procedure can be summarised as follows:

1. Choose an initial turbine density function, $d^{(i)}(x)$ (e.g. one that takes the value zero across the whole domain).
2. Solve the forward problem $F(\boldsymbol{u}, \eta, d) = 0$ with the current $d^{(i)}(x)$ to obtain the corresponding velocity field $\boldsymbol{u}$ and elevation η.
3. Evaluate the functional of interest $J(\boldsymbol{u}, \eta, d)$ using the results from step 2 and the current $d^{(i)}(x)$.
4. Compute the functional gradient $dJ/d(d(x))$.
5. Check if $dJ/d(d(x))$ fulfills the optimisation termination criteria. If so, stop and output the density function $d(x)$. Otherwise, proceed to step 6.
6. Obtain an improved turbine density function $d^{(i+1)}(x)$ and go to step 2.

In computing the functional gradient $dJ/d(d(x))$ (step 4), an adjoint approach is employed based on the dolfin-adjoint library. The advantage of this method is that the required number of PDE solves is independent of the number of input parameters. Fuller explanations on the adjoint method and its implementation can be found in (Giles and Pierce, 2000; Farrell et al., 2013; Funke et al., 2014; Mitusch et al., 2019). The termination criteria is that the maximum value of the projected gradient is less than 10^{-4}. In step 6, we use a gradient-based optimisation algorithm, here specifically the L-BFGS-B quasi-Newton method (Byrd et al., 1995) implemented in SciPy (`https://docs.scipy.org/doc/scipy/reference/generated/scipy.optimize.minimize.html`), to provide an improved turbine density used in the next iteration.

2.4. Case Study

The computational domain encompasses a region around Zhoushan Islands, shown in Figure 1. The Hulu and Taohua Islands are located to the east and south of the Zhoushan Islands respectively. The Thetis mesh is generated using the gmsh (Geuzaine and Remacle, 2009) and qmesh (Avdis et al., 2018) packages within UTM zone 51. The coarsest mesh resolution is 3000 m at the open sea boundary. As noted in Funke et al. (2016), turbine-resolving mesh resolution is not essential in the computational domain when the turbines are simulated via a distributed turbine density function (namely, the 'continuous drag' method), given that we are primarily concerned here with array-scale interactions between tidal energy deployments rather than inter-array turbine effects. As a result, the finest mesh resolution around Hulu and Taohua Islands was set to 200 m, considering the scope of the study and the resolution of the available data informing the model. The total number of vertices is 27,153 and there are 46,925 triangular elements. Four tidal stream turbine arrays are chosen and shown in Figure 2. Array 1, 2 and 3 are located near Hulu Island, while Array 4 is near Taohua Island. The longitude of the domain varies from $121.7°E$ to $122.6°E$, the latitude varies from $29.5°N$ to $30.4°N$. The coastline data are obtained from

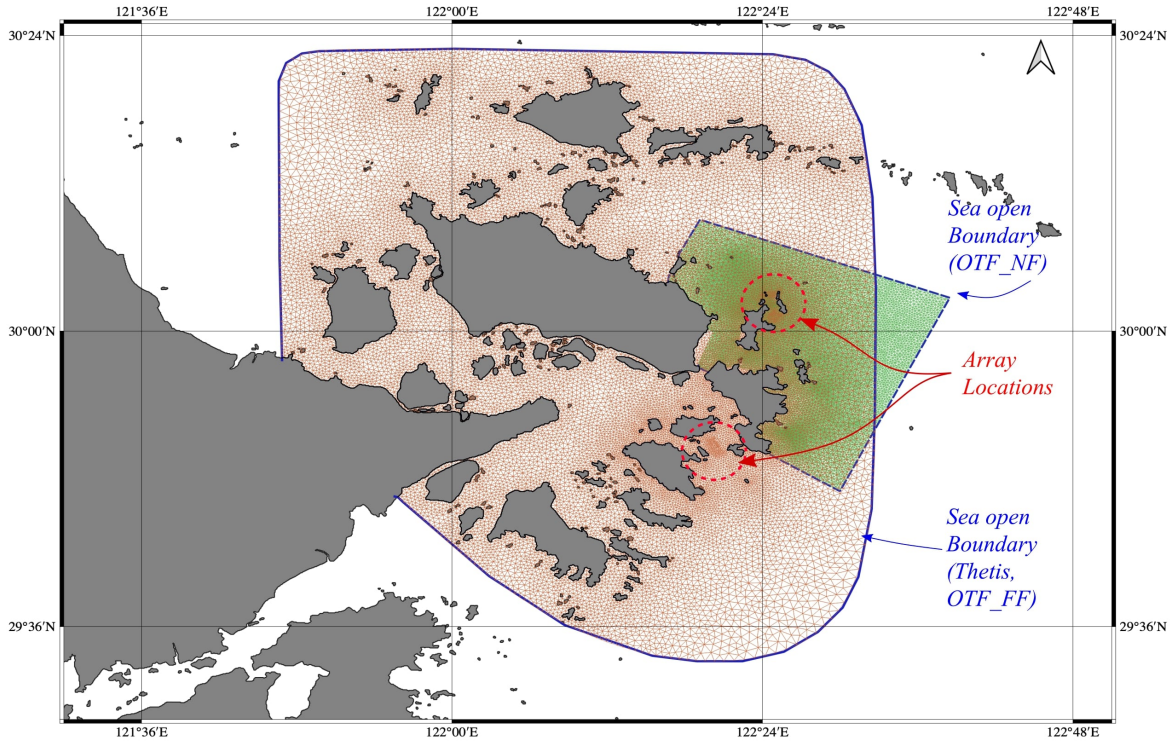

Figure 1: The location and mesh of Zhoushan Islands with the study areas of particular interest shown in red dashed circles. The dashed blue line shows the boundary of the domain for case OTF_NF, while the solid blue line represents the boundary for the OTF_FF and Thetis cases. These cases are described in more detail in section 2.4.3.

GSHHS (Wessel and Smith, 1996), adopting the finest resolution dataset available. The bathymetry data combines data from GEBCO (https://www.gebco.net/data_and_products/gridded_bathymetry_data/) (121.7° E to 122.0° E) and higher resolution measured data from the China Three Gorges Corporation (https://www.ctgbr.com.br/en/the-company/) (122.0° E to 122.6° E) in the area of interest, shown in Figure 2.

2.4.1. Boundary Conditions and Solver Options

The open boundary forcing applied here includes eight primary tidal constituents (Q_1, P_1, O_1, K_1, M_2, S_2, N_2, K_2) (Wang et al., 2017; Deng et al., 2020; Zhang et al., 2020a). The data stems from the TPXO9-atlas which comprises global, regional and local models of the barotropic tide, on a 1/30 degree resolution grid (Egbert and Erofeeva, 2002). In this work a wetting and drying algorithm is utilised at coastal boundaries. While a large number of discretisation options (finite element pairs) are possible within the *Thetis* framework, piecewise-linear discontinuous basis functions are used for both the velocity and elevation fields in this work. For temporal discretisation the backward Euler method is chosen with a constant time-step of $\Delta t = 5$ min. To avoid spurious reflections that may occur at open boundaries, a sponge layer comprising of increased viscosity and friction values is introduced. The sponge layer aims to enhance the model's stability with little effect on the simulation results in the interior areas of primary interest. The viscosity and Manning coefficients, at the open boundaries, are set to be 1000 m^2 s^{-1} and 0.1 $s/m^{\frac{1}{3}}$ respectively. The sponge layer's width is 800 m, over which the values of viscosity and Manning coefficients are decreased linearly with distance away from the boundary. Outside of the sponge area, the viscosity coefficient value is set to be 1 m^2 s^{-1}. This approach serves as a constant eddy-viscosity based turbulence model and also ensures model stability without overly dissipating hydrodynamic structures in the finer resolution regions of the model. The Manning coefficient n is determined based on a sensitivity analysis where predictions indicate that deviations from 0.02 $s/m^{\frac{1}{3}}$ would lead to larger errors in comparison with the measured data at station B1. Therefore, we set the Manning coefficient at 0.02 $s/m^{\frac{1}{3}}$ in this paper. A similar setting can be found in Goss et al. (2018). *Thetis* is configured to represent the wetting and drying effects through the methodology described in (Kärnä et al., 2011). In the ensuing discussion, the smoothness parameter associated with this wetting and drying algorithm is set to a default value $\alpha = 0.5$ m.

2.4.2. Validation Metrics

In assessing the accuracy of the model for tidal flow simulations, observed data from two elevation and two velocity gauge stations were used to verify the model and its setup utilised in this work. The location of the four stations can be observed in Figure 2. Stations A1 and B1 comprise tidal

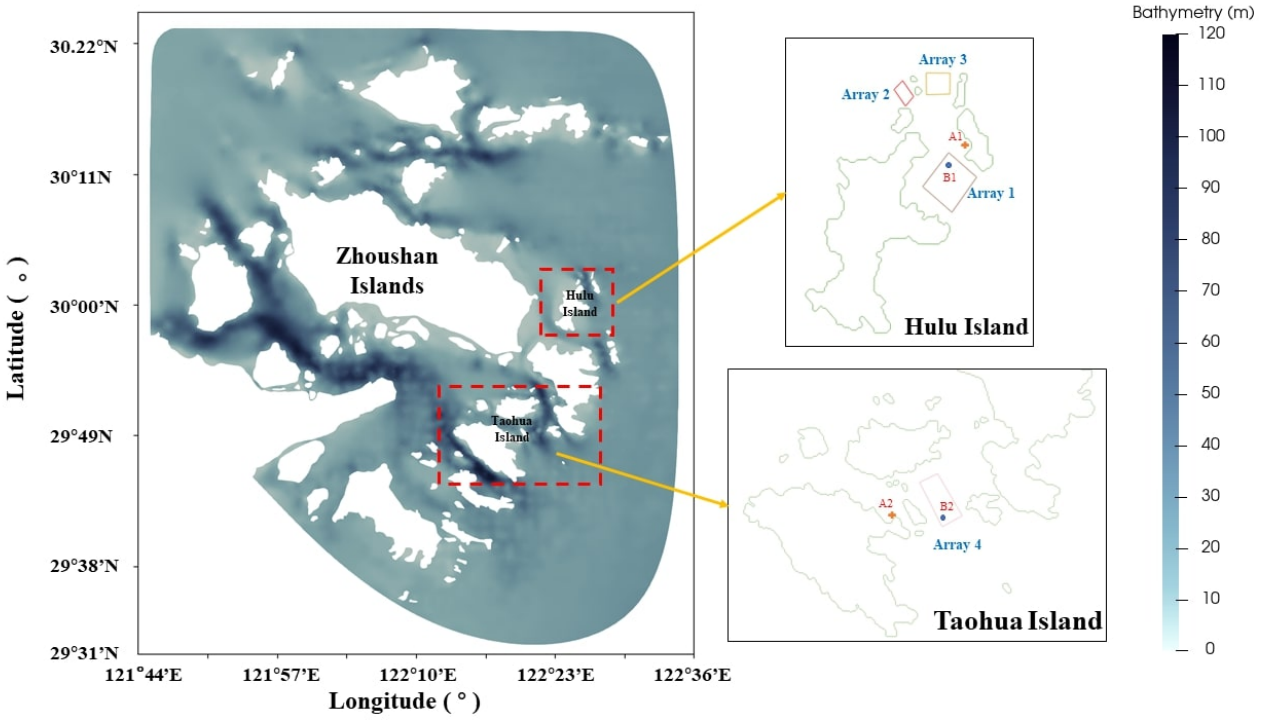

Figure 2: The bathymetry of the computational domain. Four tidal stream turbine array deployment areas are identified in blue text ("Array 1 – 4"). Two tidal elevation stations are marked with red '+' markers and "A1, A2" text, while two tidal velocity stations are marked with blue circles and "B1, B2" text.

elevation data and velocity data near Hulu Island respectively, while Stations A2 and B2 provide data near Taohua Island. The measured tidal elevation data for both A1 and A2, from 15/08/2013 to 25/08/2013, were collected hourly. The measured velocity for both B1 and B2 were collected every 10 min. They span neap, intermediate and spring tidal conditions from 16/08/2013 to 24/08/2013. The data was made available through the tidal steam energy demonstration project in Zhoushan Island, Zhejiang province.

Two metrics were used here to assess model accuracy as part of the validation exercise. The first is the R^2 (coefficient of determination) regression score. The best possible score is 1.0 and it can go negative for poor model-observation agreement. Note that a constant model would achieve an R^2 score of 0.0. R^2 is defined as:

$$R^2(y, \hat{y}) = 1 - \frac{\sum_{i=1}^{m}(y_i - \hat{y}_i)^2}{\sum_{i=1}^{m}(y_i - \tilde{y})^2}, \tag{10}$$

where $\hat{y}_i$ and y_i are the simulated value and the corresponding measured value of the i-th sample respectively, while m is the total number of the samples, and $\tilde{y} = \frac{1}{m}\sum_{i=1}^{m} y_i$ is the mean value.

The second metric is the root mean squared error (RMSE) defined as:

$$RMSE(y, \hat{y}) = \sqrt{\frac{1}{m}\sum_{i=1}^{m}((y_i - \hat{y}_i)^2)}. \tag{11}$$

2.4.3. Thetis vs OTF

In this paper, two similar cases from OTF are included to compare with *Thetis*. One of them, called OpenTidalFarm near-field (OTF_NF), is a set-up from (Zhang et al., 2020a) whose computational domain (shown in Figure 1) is smaller than the domain used in this paper. This case uses a much finer mesh due to the demands of the discrete turbine representation (Funke et al., 2014) approach that was applied in that work. Its timestep Δt is set to 30 min and viscosity coefficient is set to 10 $m^2\ s^{-1}$. The other one, called OpenTidalFarm far-field (OTF_FF), has the same set-up as was used in (Zhang et al., 2020a), but using the same domain and mesh as for the Thetis simulations conducted for this paper, see Figure 1. For the second OTF set-up (FF), the bathymetry data utilised is from GEBCO only, while *Thetis* uses the combined bathymetry data as described above. This is because OTF was found to exhibit instabilities when the bathymetry was not smoothed enough; i.e. OTF was not found to be as robust as Thetis to bathymetries with sharp gradients, as are contained in the higher resolution data from China Three Gorges Corporation. For better comparison with OTF, we also run Thetis with a timestep of 30 min.

During the validation of elevation for which observation data is hourly, all numerical results are subsampled, i.e. the numerical solution at the appropriate time levels are extracted from the full time series. For velocity which has an observational frequency of 10 min, for model runs with a coarser temporal resolution the observational data is subsampled, i.e. every third observation is used for the runs

with $\Delta t = 30$ min. For the case where the numerical time step size is $\Delta t = 5$ min, we average six time levels so that the comparison is also made at a 30 min frequency.

2.4.4. Optimisation Model Verification

As the optimisation model is gradient-based, it is important to verify the accuracy of the gradient computation determined through the adjoint method. For a detailed description of the adjoint method, we refer the reader to (Giles and Pierce, 2000; Funke, 2013; Schwedes et al., 2017). The Taylor remainder convergence test is applied to confirm the correct gradient computation, which is formulated as:

$$|\tilde{J}(m+h\delta m) - \tilde{J} - h\delta m \nabla \tilde{J}| = \mathcal{O}(h^2) \quad \text{as} \quad h \to 0, \quad (12)$$

where $\tilde{J}(m)$ is the reduced functional of interest derived from (8), i.e. the functional of interest considered as a pure function of the control parameter m. δm is a fixed but arbitrary choice of perturbation to the control variables, with h a scaling factor to change the size of this perturbation and which takes a series of values in order to assess convergence. For the gradient computation to be correct, for sufficiently small h the Taylor remainder must decrease as $\mathcal{O}(h^2)$.

All optimisation procedures carried out in the following sections have been verified using the test described in section 2.4.4. To reduce the computational expense, the optimisation algorithm was limited to five time steps for the forward model when testing the order of the Taylor remainder convergence. As all the test results demonstrated convergence values of around 1.99, we thus consider the gradient computation to be implemented correctly.

2.4.5. Tidal Array Optimisation Sequence

The channels around both Hulu and Taohua Island possess strong tidal currents which means an abundance of tidal stream energy resource is available at both locations. However, it is important to examine whether deploying turbines in one location has potential impacts on others, and whether an optimal design exits to exploit tidal stream power generation across these locations. Accordingly, the validated model is used to investigate the competition effect of multi-arrays and potential hydro-environmental impacts. Four specific areas are chosen as the turbine deployment sites: three arrays (Arrays 1, 2 and 3) are located around Hulu Island, with the fourth (Array 4) near Taohua Island as indicated in Figure 2. The initial condition for the turbine density was set to zero everywhere as per the methodology described previously. The optimisation iteratively attempts to find a series of improved turbine density distributions which yield increased energy output. During the optimisation, the forward model is initialised using spun-up ambient velocity and elevation fields obtained from the validation exercise. The diameter of the deployed turbines is assumed to be 18 m and the thrust coefficient is taken as 0.8. The maximum turbine density is defined as $(2D \times 2D)^{-1}$, based upon assuming a $2D$ minimum distance between turbines in each lateral direction.

Firstly, we study the competition effects between turbine arrays around Hulu and Taohua Island, and their impacts on the tidal elevation and velocity. The intermediate tide is simulated and different optimisation scenarios are considered to study competition and hydro-environmental impacts. The simulation starts at 14:00, 19 August 2013 and runs for 13 hrs to cover a 12.42 hrs M2 period. The optimisation and deployment scenarios considered here are:

1. optimise Arrays 1–3 simultaneously while no turbines are deployed in Array 4 around Taohua Island;
2. optimise Array 4 while no turbines are deployed in Arrays 1–3 around Hulu Island;
3. optimise the four turbines arrays around Hulu and Taohua Island simultaneously;
4. deploy turbines in both Array 1–3 and Array 4 using the optimised designs obtained under scenarios 1 and 2 respectively.

In addition, the study also focuses on the competition between the three arrays around Hulu Island during different tidal periods. These arrays are optimised under the following scenarios:

1. optimise Array 1 while no turbines are deployed in Arrays 2–3;
2. optimise Arrays 2–3 while no turbines are deployed in Array 1;
3. optimise Array 1 while turbines in Arrays 2–3 are deployed based on scenario 2;
4. optimise Arrays 2–3 while turbines in Array 1 are deployed based on scenario 1;
5. optimise all three turbine arrays simultaneously;
6. deploy turbines in both Array 1 and Arrays 2–3 using the optimised designs obtained under scenarios 1 and 2 respectively.

3. Hydrodynamic Model Validation and Intercomparison

3.1. Tidal Elevation Validation

Figure 3(a) presents a comparison of measured (solid points) and simulated data (solid line) at the tidal elevation station A1. To demonstrate the improvement obtained with *Thetis*, two simulation results obtained with OpenTidalFarm (OTF), a forerunner of *Thetis*, are included: OTF_NF a setup from (Zhang et al., 2020a) which uses a smaller domain (see figure 2), and OTF_FF which uses the same domain and mesh as the Thetis results. It is observed that the simulation results for elevation from all cases agree well with the observations. The R^2 regression scores for these cases (all beyond 0.97) support the simulations' accuracy. However, some differences are observed in RMSE value, the OTF_FF has the lowest value at 0.121 m. *Thetis* and OTF_NF have the same value at 0.149 when simulating tidal elevations at location A1. More details about the value of the R^2 regression score and RMSE can be found in Table 1.

Figure 3(b) shows the comparison between measured (solid points) and simulated (solid line) tidal elevations around Taohua Island at A2. As OTF_NF has a smaller computational

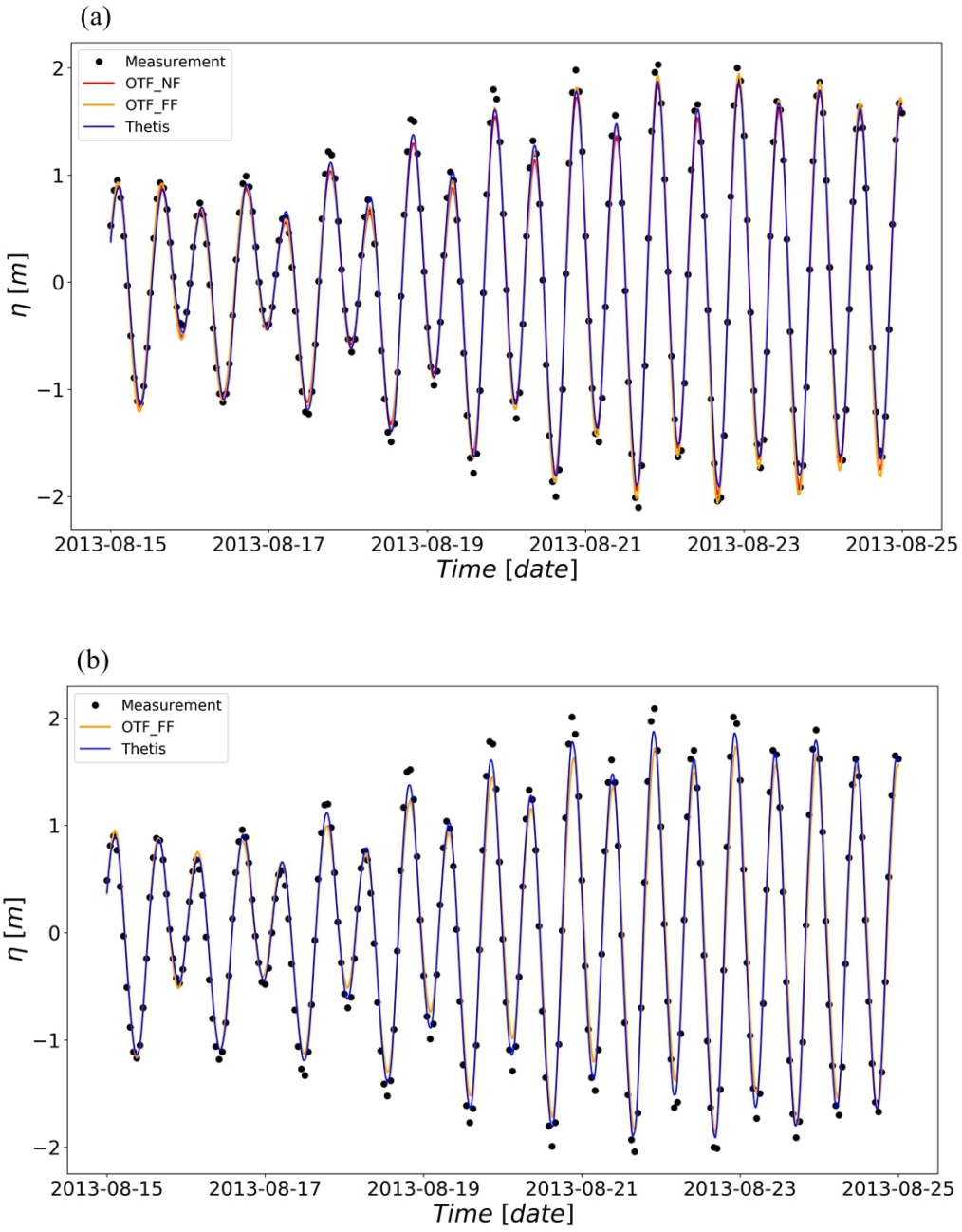

Figure 3: Comparison between measured and simulated tidal elevation at the tidal elevation stations. (a): Station A1 around Hulu Island, (b): Station A2 around Taohua Island.

domain, it does not include the station A2. So only results from *Thetis* and OTF_FF are compared here. It can be seen clearly that *Thetis* has a more satisfactory agreement than OTF_FF. The R^2 regression score and RMSE for *Thetis* are 0.979 and 0.142 m respectively. More details about the value of the R^2 regression score and RMSE can be found in Table 2.

3.2. Tidal Velocity Validation

Comparison of the measured and simulated tidal stream velocity magnitude and direction at station B1 near Hulu Island can be seen in Figure 4(a, b). The results from OTF are also included. Simulation results indicate a satisfactory agreement with measurements, with the results from *Thetis* generally showing a clear improvement in accuracy over the previous OTF results in terms of the velocity magnitudes. Comparing the R^2 regression score of OTF_NF with *Thetis*, we observe an improvement from 0.620 (OTF_NN) to 0.715

(Thetis) among the neap tide, from 0.798 to 0.852 among the intermediate tide and from 0.709 to 0.814 among the spring tide. Similar trends can be seen for the RMSE results. During the neap tide, the RMSE decreases by 13.7% (from 0.146 m/s to 0.126 m/s). For the intermediate and spring tides, the reductions are 14.4% (from 0.174 m/s to 0.149 m/s) and 20.0% (from 0.245 m/s to 0.196 m/s) respectively. Among all these three periods, the use of *Thetis* has improved the overall R^2 regression score from 0.709 (obtained with OTF) to 0.794 and reduced the overall RMSE value from 0.188 m/s to 0.157 m/s. As for the velocity direction, the R^2 regression score is not considered as it is meaningless to calculate the average direction. The velocity direction RMSE results of OTF, among all these three tides, are slightly smaller than that of *Thetis*. More details about the statistics can be found in Table 1.

Figure 4(a, b) demonstrates that the simulated tidal velocity from *Thetis* is in favourable agreement with the measured velocity. However, some discrepancy exists. The reasons for such errors can be attributed to several factors: (1) a uniform Manning coefficient is used for the whole domain, which should really vary subject to the real world physical seabed conditions; (2) the bathymetry data resolution may not be sufficient, especially given the sharp water depth gradients around Hulu Island, which may lead to some errors in the representation of certain bathymetry-induced flow structures; (3) the effects of wind forcing and other atmospheric factors are not considered in our modelling, which is expected to lead to some additional deviations; and (4) we employ a depth-averaged modelling approach for what might be fundamentally a 3D flow problem in certain parts of the domain. Furthermore, measurement errors also arise due to harsh conditions beyond our control in the marine environment, which can then lead to a disagreement with the numerical results.

Less ideal agreement is seen in Figure 5(a, b). Although the RMSE values are acceptable, the R^2 scores for the neap and spring tide are 0.126 and 0.469 respectively. Apart from the reasons acknowledged so far, this may also be partly due to the fact that: (1) Taohua Island (where gauge B2 is located) is surrounded by many smaller islands, which makes the actual marine environment very complicated to resolve with the mesh and data resolution available for this study; (2) due to computational constraints, some small islands which require a very high-resolution mesh in order to properly capture their shapes were ignored in this model set-up, and this may contribute to some errors; (3) the uniform Manning coefficient value chosen was based on the sediment size around Hulu Island, which may not be representative for the simulation around Taohua Island. Considering the above, only the simulation during the intermediate tidal period around Taohua Island is discussed and analysed in this paper. Comparison metrics are summarised in Table 2.

Note For fairer comparison with the OTF results, as well as using $\Delta t = 5$ min we also run *Thetis* with a timestep of 30 min. The increase in timestep causes a small difference in validation metrics (see Table 1 and 2), but the results are still better than those of OTF. The optimisation results presented in the rest of this paper are based on the Thetis runs at a 5 min timestep.

4. Optimisation Results and Competition Effects

4.1. Competition Effect between Arrays around Hulu and Taohua Island

Figure 6 shows the optimised results for the first three scenarios. Scenario 4 combines the optimised turbine density of scenario 1 (Figure 6(a)) and 2 (Figure 6(b)) and is therefore not repeated. It is seen that there is little difference between the turbine density around Hulu Island between scenarios 1 and 3. As for scenarios 2 and 3, only slight changes are observed at the array's northwest corner around Taohua Island. The average power generated during the intermediate tide from each scenario is listed in Table 3. Scenario 4 yields an average output of 73.63 MW. This is only slightly lower than the 73.70 MW obtained in scenario 3 which optimises all arrays simultaneously. This suggests that the competition effects between the arrays located at Hulu and Taohua Island is effectively negligible during the intermediate tide. As such, considering the arrays' optimisation individually or simultaneously makes little difference.

It is also worth noting that the individual arrays' power outputs under scenario 4 are slightly higher than the equivalent scenario 1 and 2 values. This implies that these arrays have a broad but slightly affected area, and that they could benefit from the presence of one another marginally even without joint optimisation.

The influence of the arrays on tidal elevation and velocity magnitude is also investigated. The maximum change in the tidal elevation during the intermediate tide is 0.15 m which is relatively small. The change in the peak tidal velocity caused by the turbine arrays over the flood/ebb periods are shown in the left and right columns of Figure 7 respectively. It can be observed that arrays around Hulu Island have little effect on the tidal velocity around Array 4, and vice versa. This provides further evidence for the lack of competition effects between the arrays around Hulu and Taohua Island during the intermediate tide. In the near field, around both Hulu and Taohua Island, significant decreases in velocity can be observed within the turbine array plots, while clear increases in velocity are seen in the bypass flow at the sides of the arrays as well as in channels adjacent to the turbine deployment areas as flow gets redirected due to the added resistance, or blockage, introduced by the turbines. Figure 7(c) shows that the tidal velocity in the immediate wake area downstream of the turbine array is reduced the most. In Figure 7(e), the tidal velocity at either side of Array 4 doubles to approximately 3m/s. In terms of far field effects, the turbine arrays around Hulu Island have a relatively smaller affected area. The impacted area due to the turbine array around Taohua Island is more significant, with a noticeable change observed at the southwest corner of Zhoushan Islands. There is

Table 1
Statistical metrics describing agreement between the simulated and observed time series data at A1/B1 (T_5: *Thetis* results with 5 min timestep. T_{30}: *Thetis* results with 30 min timestep. O_N: OTF_NF. O_F: OTF_FF).

Period	Types	RMSE				R2 score			
		T_5	T_{30}	O_N	O_F	T_5	T_{30}	O_N	O_F
All (2013.8.15 – 2013.8.25)	Water elevation η (m)	0.149	0.180	0.149	0.121	0.977	0.965	0.977	0.986
Neap tide (2013.8.16 10:00 – 2013.8.17 11:00)	Velocity magnitude u (m/s)	0.126	0.103	0.146	0.176	0.715	0.810	0.620	0.442
	Current direction θ (°)	44.356	32.999	42.198	29.439	-	-	-	-
Intermediate tide (2013.8.19 14:00 – 2013.8.20 15:00)	Velocity magnitude u (m/s)	0.149	0.135	0.174	0.301	0.852	0.880	0.798	0.398
	Current direction θ (°)	20.948	19.443	12.733	24.859	-	-	-	-
Spring tide (2013.8.23 10:00 – 2013.8.24 11:00)	Velocity magnitude u (m/s)	0.196	0.233	0.245	0.396	0.814	0.736	0.709	0.240
	Current direction θ (°)	32.027	21.929	23.098	30.148	-	-	-	-
All (2013.8.15 – 2013.8.25)	Velocity magnitude u (m/s)	0.157	0.157	0.188	0.291	0.794	0.809	0.709	0.360
	Current direction θ (°)	32.444	24.790	26.010	28.149	-	-	-	-

Table 2
Statistical metrics describing agreement between the simulated and observed time series data at A2/B2 (T_5: *Thetis* results with 5 min timestep. T_{30}: *Thetis* results with 30 min timestep. O_F: OTF_FF).

Period	Types	RMSE			R2 score		
		T_5	T_{30}	O_F	T_5	T_{30}	O_F
All (2013.8.15 – 2013.8.25)	Water elevation η (m)	0.142	0.169	0.216	0.979	0.970	0.946
Neap tide (2013.8.16 10:00 – 2013.8.17 11:00)	Velocity magnitude u (m/s)	0.236	0.181	0.231	0.126	0.490	0.041
	Current direction θ (°)	47.527	37.057	47.921	-	-	-
Intermediate tide (2013.8.19 14:00 – 2013.8.20 15:00)	Velocity magnitude u (m/s)	0.216	0.212	0.427	0.726	0.735	-0.211
	Current direction θ (°)	40.251	32.401	40.463	-	-	-
Spring tide (2013.8.23 10:00 – 2013.8.24 11:00)	Velocity magnitude u (m/s)	0.261	0.339	0.514	0.469	0.102	-0.285
	Current direction θ (°)	32.534	37.412	35.948	-	-	-
All (2013.8.15 – 2013.8.25)	Velocity magnitude u (m/s)	0.238	0.244	0.391	0.440	0.442	-0.152
	Current direction θ (°)	40.104	35.623	41.444	-	-	-

Table 3
Average power generated (Avg P) in each scenario.

Avg P (MW)	Scenario 1	Scenario 2	Scenario 3	Scenario 4
Hulu	30.95	0	31.04	31.04
Taohua	0	42.54	42.66	42.60
all	30.95	42.54	73.70	73.63

no significant difference for the changes in tidal velocity between Figure 7(a,c) and the combined result of Figure 7(e). A similar result can also be observed between Figure 7(b, d, e), which again illustrate that the turbine arrays around Hulu and Taohua Island have no significant interactions.

4.2. Competition Effect between Array 1 and Arrays 2–3 around Hulu Island

For this case different tidal periods are also considered in order to check the sensitivity of the optimal turbine density to neap (starting 10:00, 16 August 2013), intermediate (starting 14:00, 19 August 2013) and spring (starting 10:00, 23 August 2013) conditions. All time intervals considered span 13h, as previously.

Figure 8(a, b) shows the optimised results under scenarios 1 and 2 for three different tidal periods. During the neap tide, turbines appear to fully cover the entire area as the tides are relatively slow and increasing the turbine number is the only way to increase the energy output. The optimised results from the intermediate tide and spring tide are similar. Results confirm that the optimised configurations are consistent when the tidal velocity is large enough. A point that should be highlighted here is that in this model set-up cut-in and cut-out speeds are not considered for simplicity, but these can be easily included. The average power generated and the number of turbines in the arrays is listed in Table 4.

Figure 8 also shows the optimised results when Arrays 1–3 are all deployed with turbines (scenarios 4–6). By comparing the result from scenarios 3 and 4 against scenario 5, it is found that the optimised arrays show similar turbine density distribution patterns. For example, Array 1 in scenario 3 is optimised and its result is similar to that in scenario 5 over

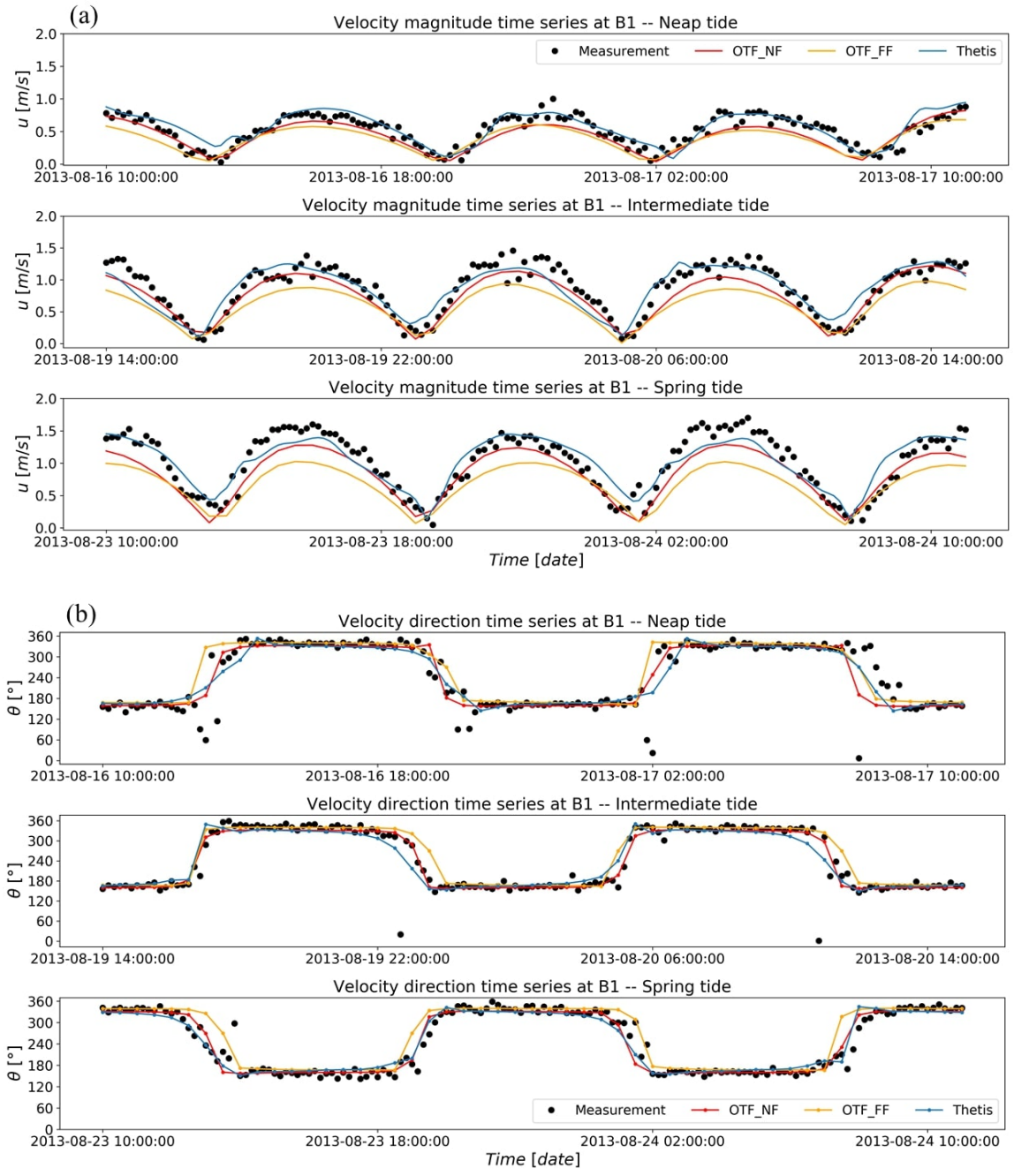

Figure 4: Comparison between measured and simulated tidal stream velocity (magnitude and direction) at the tidal elevation station B1.

each time interval considered. Even though Arrays 2–3 in scenario 3 have different turbine density distributions than scenario 5, their average power generated is almost identical (4.57 MW and 4.46 MW respectively). They therefore have a similar environmental influence to Array 1 and the optimised results of Array 1 in scenarios 3 and 5 are nearly the same. A similar situation can be found when comparing Arrays 2–3 in scenarios 4 and 5 for the same reason.

According to the comparison of average power (Table 4) between scenarios 1–2 and scenario 6, a strong competition effect is found between Array 1 and Arrays 2–3. When optimising Array 1 alone during spring tide (scenario 1), the average power is 38.98 MW which is the highest among the three tides. For Arrays 2–3 it is 34.61MW (scenario 2). However, when combining these two optimised results (scenario 6), Array 1 only generates 30.56 MW, a decrease of 21.5%. The average power generated by Arrays 2–3 drops to 20.00 MW, a decrease of 42.2%. Similar significant decreases due to competition effects can also be found during the neap and intermediate tides.

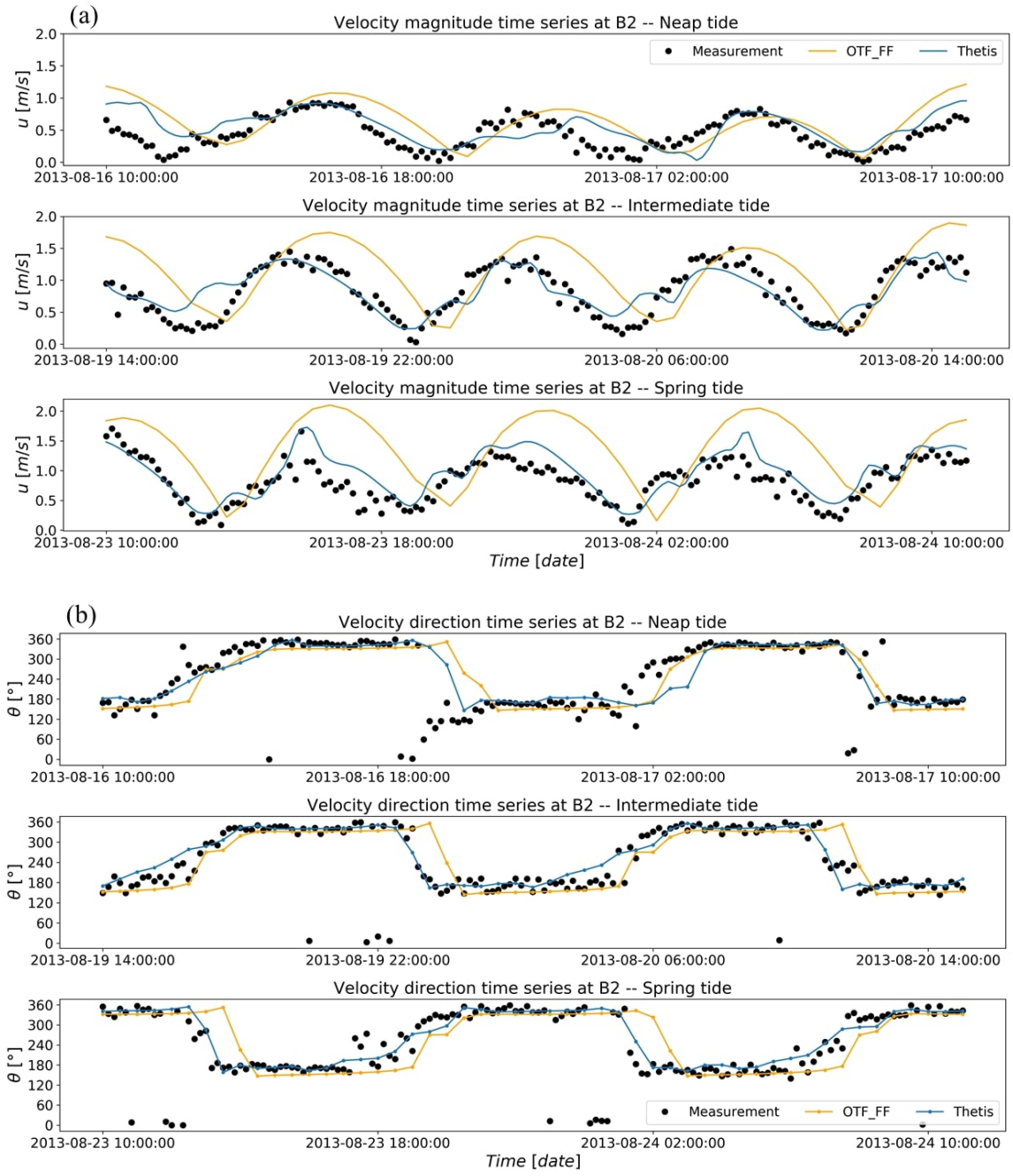

Figure 5: Comparison between measured and simulated tidal stream velocity (magnitude and direction) at the tidal elevation station B2.

Scenarios 3 and 4 investigate the influence of the order in which optimisation occurs. Table 4 shows that the optimised results in these two scenarios have almost identical average power yields for all tidal periods. However, they all have a slight improvement compared to scenario 6. For instance, during the spring tide, the total Avg P of scenario 3 is 51.02 MW, which is slightly larger than the 50.59 MW obtained in scenario 6. This confirms that in terms of the total Avg P, the order of deploying these arrays does not play an important role.

For scenarios 3–5, it can be seen that the optimised results contain fewer turbines compared with scenario 6 but obtain a larger total Avg P. Scenario 5, which, as expected, has the highest total Avg P, decreases the number of turbines from 1968 to 1606, i.e. an 18.4% reduction. Recall the optimisation here has been configured to maximise the total Avg P by changing the density, i.e. the number and position of the turbines in the array. When higher total Avg P is obtained by reducing the number of turbines, it means the higher number is beyond the optimal value. This agrees with the principle

Table 4
The average power generated (Avg P) and the number of turbines (N_t) in the optimised result of each scenario during the three tidal periods considered.

Scenarios & Array names		Neap tide Avg P (MW)	N_t	Intermediate tide Avg P (MW)	N_t	Spring tide Avg P (MW)	N_t
Scenario 1	Array 1	9.02	1435	24.03	1397	38.98	1400
Scenario 2	Arrays 2–3	7.11	627	20.18	568	34.61	567
	Array 1	7.08	1324	17.95	1113	29.13	1114
Scenario 3	Arrays 2–3	4.57	627	12.87	568	21.89	567
	All	11.65	1951	30.83	1681	51.02	1682
	Array 1	7.34	1435	19.35	1397	31.55	1400
Scenario 4	Arrays 2–3	4.33	530	11.38	478	19.33	483
	All	11.68	1965	30.73	1875	50.87	1884
	Array 1	7.24	1319	18.49	1110	30.03	1119
Scenario 5	Arrays 2–3	4.46	529	12.46	480	21.19	486
	All	11.70	1849	30.95	1590	51.22	1606
	Array 1	7.17	1435	18.79	1397	30.59	1400
Scenario 6	Arrays 2–3	4.46	627	11.82	568	20.00	567
	All	11.63	2062	30.61	1965	50.59	1968

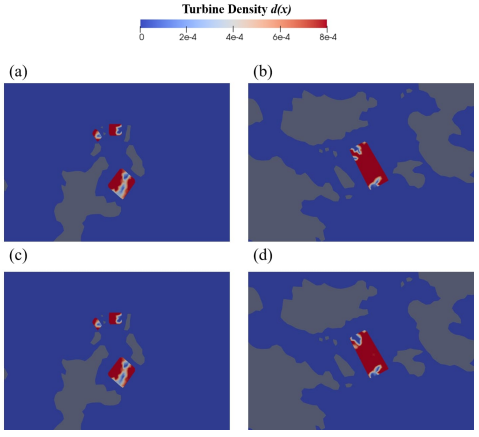

Figure 6: Optimised turbine density for different arrays under scenarios 1, 2 and 3. (a): scenario 1: optimisation of the three arrays around Hulu island, with no turbine in the Taohua island array (b): scenario 2: optimisation of the Taohua island array, with no turbines near Hulu island (c) and (d): scenario 3: simultaneous optimisation of the the three arrays near Hulu Island and one array near Taohu island.

that the total Avg P first increases with number of turbines but at some point may start to decrease due to global blockage effects, i.e. the flow being redirected.

The average power generated per turbine (Avg P/N_t) is shown in Figure 9. It is seen that although Array 1 always has a higher total Avg P, Arrays 2–3 are much more effective than Array 1. For instance, in scenarios 1 and 2, the Avg P/N_t of Array 1 is less than half that of Arrays 2–3.

Comparing scenarios 1 and 2 with 6, strong competition effects are found between Array 1 and Arrays 2–3. If competition effects are not considered prior to developing tidal stream energy in this area, and Array 1 and Arrays 2–3 are optimised respectively, the total energy output would reduce significantly and a very low Avg P/N_t would result. Considering the order of optimisation would improve the total energy output and decrease costs, but optimising Array 1 and Arrays 2–3 simultaneously would be the best choice. Although it would not greatly weaken the competition effect, it can significantly reduce the number of turbines installed overall while generating equivalent power.

5. Discussion

Based on the validation results presented in sections 3.1 and 3.2, the superiority of *Thetis*' simulation capabilities over OpenTidalFarm is confirmed. Results from *Thetis* show far better agreement with measurement in the velocity magnitude compared with the result from two OTF sets of results. For the water elevation, *Thetis*' result is equivalent to OTF_NF's result, both of which are acceptable. Although OTF_FF has the best agreement with measured data for the water elevation at station A1, its results for the other three stations have higher errors. This may be because the bathymetry data obtained from GEBCO are not sufficient to capture the sharply changing water depth in the computational domain. For the velocity direction, *Thetis* results have higher RMSE values compared with the two OTF results at station B1, but are acceptable. In Figure 4, it can be seen that the primary differences between the measured and simulated velocity direction occur when the velocity magnitude is close to zero. As the tidal stream energy is proportional to the cube of the tidal current velocity magnitude, these difference in velocity direction would cause little effect. Furthermore, it should be pointed out again that the OTF set-up from (Zhang et al., 2020a) used a much larger viscosity value; specifically the viscosity value was set to 10 m^2/s in OTF to ensure the model's stability. In contrast, improvements in *Thetis* allow stability for lower values of viscosity; here a value of $\upsilon_t = 1$ m^2/s is used. Setting viscosity to $\upsilon_t = 10$ m^2/s leads to unre-

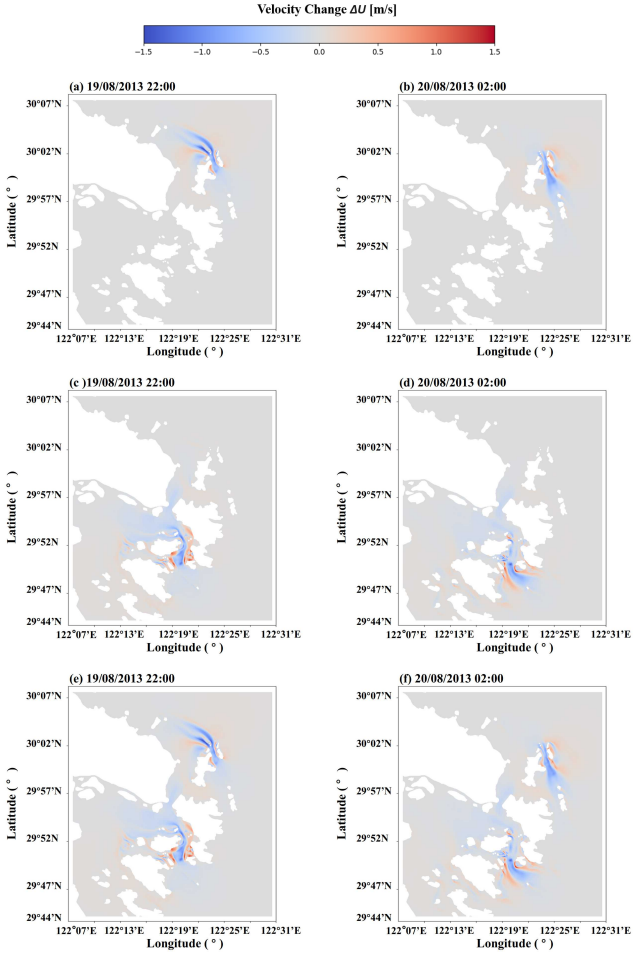

Figure 7: Changes in velocity magnitude around Hulu and Taohua Island in each scenario. The figures in the left column is during the flood tide, while in the right column is during the ebb tide.

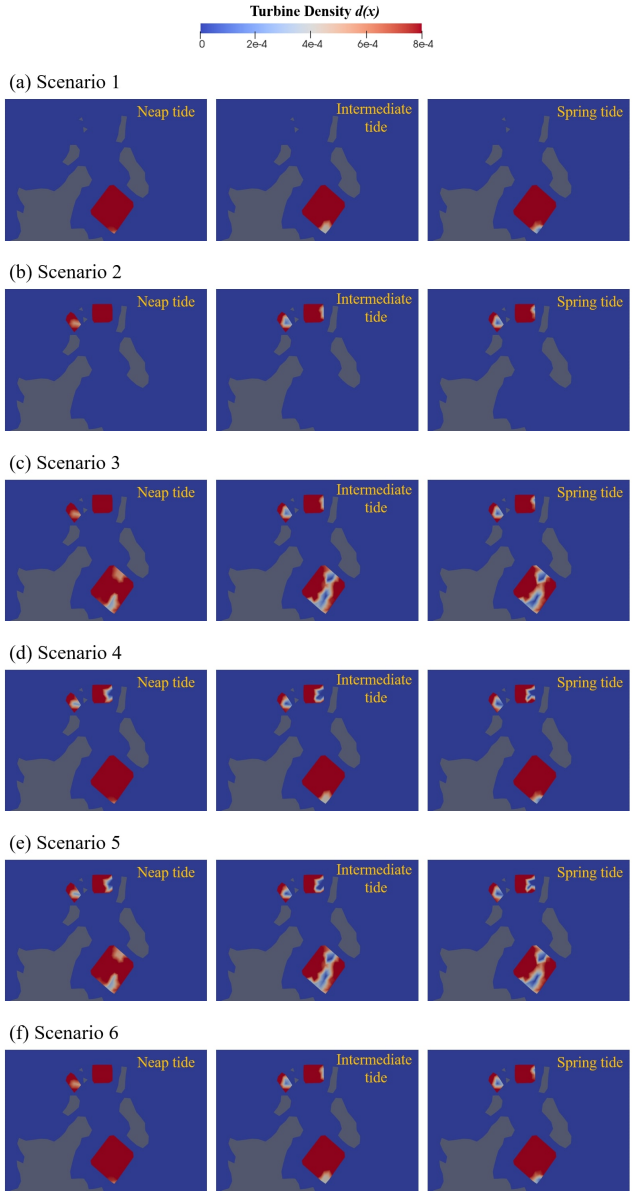

Figure 8: Optimised turbine densities for the three arrays around Hulu Island for the six scenarios and the three tidal intervals considered.

alistic mixing and the dissipation of hydrodynamic features in finely resolved areas of relevance to tidal stream energy. Additionally, *Thetis* can be considered an improved far-field model in that it is more robust not only in terms of required viscosity levels but also in terms of its abilities to cope with sharp gradients in fields such as bathymetry. Therefore, an improved discretisation method, a lower viscosity coefficient and a larger simulation area in *Thetis* lead to a better agreement with the measurement than that of the OTF model set-up from (Zhang et al., 2020a).

The reason for the lack of competition effects between the arrays around Hulu and Taohua Island are largely due to the distance, the maximum size of these array deployments, as well as the large number of islands and the geometric complexity between Hulu and Taohua Island which weakens the connection between the hydrodynamic interactions at the two sites.

Wake effects around Taohua Island are preserved over a greater area than that around Hulu Island. This may be because around Hulu Island the undisturbed flow from the adjacent waters accelerates array wake recovery, while around Taohua Island, the low turbulence in the vicinity does not promote mixing and thus a swift recovery.

The optimisation result obtained by considering a functional based on total Avg P only results in a large number of turbines. This may clearly not be optimal economically, as the number of turbines is intimately related to the array cost. Therefore, when considering the economic benefits, the Avg P/N$_t$ can be an important factor and should be incorporated in the analysis. In *Thetis* it is relatively straightforward to incorporate an economic model and run a multi-objective optimisation (Goss et al., 2018; Culley et al., 2016; Goss et al., 2020). However, as specific economic data was lacking this approach was not considered here but will be followed up on in future work.

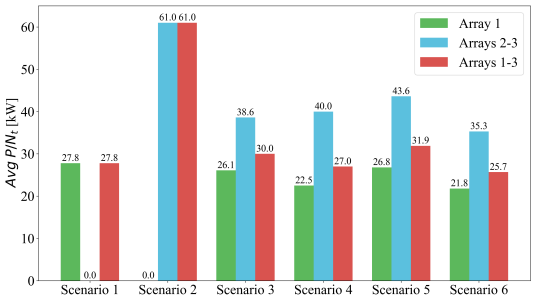

Figure 9: The average power generated per turbine (Avg P/N_t) in the optimised result for each scenario during spring tide.

6. Conclusions

In this paper a two-dimensional numerical model is set up using the *Thetis* coastal ocean modelling framework. The model is validated using data collected from two tide gauge elevation stations and two velocity stations around Zhoushan Islands. By comparing the results obtained with those from the preceding *OpenTidalFarm* (OTF) software, it is confirmed that *Thetis* exhibits improved stability and accuracy properties, which is expected due to its improved discretisation methods. Multi-arrays around Hulu and Taohua Island are subsequently optimised using a continuous array representation approach and gradient-based methods in order to maximise the average power output across all arrays. Under different optimisation scenarios and tidal periods, the competition effects between the arrays and the hydrodynamic impacts caused by the arrays are studied.

Results indicate that there is no clear competition effect between an array near Taohua Island with three potential arrays near Hulu Island. Optimising them individually and simultaneously leads to almost identical results. This is likely due to the sufficient intermediate distance as well as the multiple islands between Hulu and Taohua islands which weaken any interactions. The impact of the arrays on tidal elevation is minimal with a maximum change in elevation only 0.75% of the average depth. In the near field, a significant decrease in velocity magnitude is found within the turbine array plots while clear increases can be seen in the bypass flows to the sides of the arrays and in adjacent channels. In the far field, the impact caused by the arrays around Hulu Island recovers more quickly than that around Taohua Island. This may be because the islands to the northwest of Taohua Island strengthen the array's influence.

The optimised results for the three representative (neap, intermediate and spring) tidal periods considered for the three more closely positioned arrays around Hulu island tell a different story. During neap tides when the tidal velocity is small, increasing the number of turbines is the only way to increase the average power. Similar optimisation results are observed during spring and intermediate tidal periods. Significant competition effects are found between the three turbine arrays around Hulu Island. If Array 1 and Arrays 2–3 rely on optimal designs obtained in isolation, a decrease up to 42% in the average power is found for Array 2–3 during the spring tides when these designs are then deployed simultaneously. When considering the order of array optimisation, firstly optimising Array 2–3 is slightly better than optimising Array 1 first in terms of the total average power. However, optimising all three arrays simultaneously is the best strategy, improving the total average power the most relative to alternative cases.

The limitations of only considering total average power (Avg P) is found by comparing the average power per turbine (Avg P/N$_t$) between Array 1 and Arrays 2–3. The optimised result could be very costly from an economic perspective. In future work considering a multi-optimisation model which optimises for both total Avg P and Avg P/N$_t$ would be suggested to address this.

This study shows that competition effects can be weakened through the presence of complex features such as islands. When multi-arrays are being considered where competition effects may be strong, it is important to optimise prospective designs in tandem.

Acknowledgements

The authors are grateful for sponsorship from China Scholarship Council (No. 201906710084), the National Natural Science Foundation of China (51879098), and the Marine Renewable Energy Research Project of State Oceanic Administration (GHME2015GC01). The authors also acknowledge the support of the UK's Engineering and Physical Sciences Research Council under projects EP/R029423/1 and EP/R007470/1.

CRediT authorship contribution statement

Jisheng Zhang: Conceptualization, Investigation, Resources, Writing - review & editing, Supervision, Funding Acquisition. **Can Zhang:** Methodology, Validation, Formal analysis, Writing - Original Draft. **Athanasios Angeloudis:** Methodology, Formal analysis, Writing - Original Draft. **Stephan C. Kramer:** Validation, Software, Writing - review & editing. **Rui He:** Investigation, Writing - Original Draft. **Matthew D. Piggott:** Conceptualization, Methodology, Resources, Writing - review & editing, Supervision, Funding Acquisition.

References

Ahmadian, R., Falconer, R., Bockelmann-Evans, B., 2012. Far-field modelling of the hydro-environmental impact of tidal stream turbines. Renewable Energy 38, 107–116.

Angeloudis, A., Kramer, S.C., Avdis, A., Piggott, M.D., 2018. Optimising tidal range power plant operation. Applied Energy 212, 680 – 690. URL: http://www.sciencedirect.com/science/article/pii/S0306261917317671, doi:https://doi.org/10.1016/j.apenergy.2017.12.052.

Angeloudis, A., Kramer, S.C., Hawkins, N., Piggott, M.D., 2020. On the potential of linked-basin tidal power plants: An operational and coastal

modelling assessment. Renewable Energy 155, 876–888. doi:https://doi.org/10.1016/j.renene.2020.03.167.

Avdis, A., Candy, A.S., Hill, J., Kramer, S.C., Piggott, M.D., 2018. Efficient unstructured mesh generation for marine renewable energy applications. Renewable Energy 116, 842–856.

Bai, G., Li, J., Fan, P., Li, G., 2013. Numerical investigations of the effects of different arrays on power extractions of horizontal axis tidal current turbines. Renewable Energy 53, 180–186.

Baker, A.L., Craighead, R.M., Jarvis, E.J., Stenton, H.C., Angeloudis, A., Mackie, L., Avdis, A., Piggott, M.D., Hill, J., 2020. Modelling the impact of tidal range energy on species communities. Ocean & Coastal Management 193, 105221. URL: http://www.sciencedirect.com/science/article/pii/S0964569120301319, doi:https://doi.org/10.1016/j.ocecoaman.2020.105221.

Byrd, R.H., Lu, P., Nocedal, J., Zhu, C., 1995. A limited memory algorithm for bound constrained optimization. SIAM Journal on scientific computing 16, 1190–1208.

Chen, W.B., Liu, W.C., Hsu, M.H., 2013. Modeling evaluation of tidal stream energy and the impacts of energy extraction on hydrodynamics in the taiwan strait. Energies 6, 2191–2203.

Chen, Y., 2015. Study on the effects of tidal turbine and array on the flow field [D]. Ph.D. thesis. Doctoral Thesis, Beijing, China: Tsinghua University, 2015 (in Chinese).

Culley, D., Funke, S., Kramer, S., Piggott, M., 2016. Integration of cost modelling within the micro-siting design optimisation of tidal turbine arrays. Renewable Energy 85, 215–227.

De Dominicis, M., Murray, R.O., Wolf, J., 2017. Multi-scale ocean response to a large tidal stream turbine array. Renewable Energy 114, 1160–1179.

Defne, Z., Haas, K.A., Fritz, H.M., Jiang, L., French, S.P., Shi, X., Smith, B.T., Neary, V.S., Stewart, K.M., 2012. National geodatabase of tidal stream power resource in usa. Renewable and Sustainable Energy Reviews 16, 3326–3338.

Deng, G., Zhang, Z., Li, Y., Liu, H., Xu, W., Pan, Y., 2020. Prospective of development of large-scale tidal current turbine array: An example numerical investigation of zhejiang, china. Applied Energy 264, 114621.

du Feu, R., Funke, S., Kramer, S., Culley, D., Hill, J., Halpern, B., Piggott, M., 2017. The trade-off between tidal-turbine array yield and impact on flow: A multi-objective optimisation problem. Renewable Energy 114, 1247 – 1257. URL: http://www.sciencedirect.com/science/article/pii/S0960148117307097, doi:https://doi.org/10.1016/j.renene.2017.07.081.

du Feu, R., Funke, S., Kramer, S., Hill, J., Piggott, M., 2019. The trade-off between tidal-turbine array yield and environmental impact: A habitat suitability modelling approach. Renewable Energy 143, 390 – 403. URL: http://www.sciencedirect.com/science/article/pii/S0960148119306251, doi:https://doi.org/10.1016/j.renene.2019.04.141.

Egbert, G.D., Erofeeva, S.Y., 2002. Efficient inverse modeling of barotropic ocean tides. Journal of Atmospheric and Oceanic Technology 19, 183–204.

Fallon, D., Hartnett, M., Olbert, A., Nash, S., 2014. The effects of array configuration on the hydro-environmental impacts of tidal turbines. Renewable Energy 64, 10–25.

Farrell, P.E., Ham, D.A., Funke, S.W., Rognes, M.E., 2013. Automated derivation of the adjoint of high-level transient finite element programs. SIAM Journal on Scientific Computing 35, C369–C393.

Funke, S., 2013. The automation of PDE-constrained optimisation and its applications. Ph.D. thesis. Imperial College London.

Funke, S.W., Farrell, P.E., Piggott, M., 2014. Tidal turbine array optimisation using the adjoint approach. Renewable Energy 63, 658–673.

Funke, S.W., Kramer, S.C., Piggott, M.D., 2016. Design optimisation and resource assessment for tidal-stream renewable energy farms using a new continuous turbine approach. Renewable Energy 99, 1046–1061.

Geuzaine, C., Remacle, J.F., 2009. Gmsh: A 3-d finite element mesh generator with built-in pre- and post-processing facilities. International Journal for Numerical Methods in Engineering 79, 1309–1331. URL: https://onlinelibrary.wiley.com/doi/abs/10.1002/nme.2579, doi:10.1002/nme.2579, arXiv:https://onlinelibrary.wiley.com/doi/pdf/10.1002/nme.2579.

Giles, M.B., Pierce, N.A., 2000. An introduction to the adjoint approach to design. Flow, turbulence and combustion 65, 393–415.

Goss, Z., Piggott, M., Kramer, S., Avdis, A., Angeloudis, A., Cotter, C., 2018. Competition effects between nearby tidal turbine arrays-optimal design for alderney race, in: Advances in Renewable Energies Offshore: Proceedings of the 3rd International Conference on Renewable Energies Offshore (RENEW 2018), October 8-10, 2018, Lisbon, Portugal, CRC Press. p. 255.

Goss, Z.L., Coles, D.S., Piggott, M.D., 2020. Identifying economically viable tidal sites within the alderney race through optimization of levelized cost of energy. Philosophical Transactions of the Royal Society A: Mathematical, Physical and Engineering Sciences 378, 20190500. URL: https://royalsocietypublishing.org/doi/abs/10.1098/rsta.2019.0500, doi:10.1098/rsta.2019.0500.

Grabbe, M., Lalander, E., Lundin, S., Leijon, M., 2009. A review of the tidal current energy resource in norway. Renewable and Sustainable Energy Reviews 13, 1898–1909.

Hammons, T., 2008. Energy potential of the oceans in europe and north america: tidal, wave, currents, otec and offshore wind. International Journal of Power and Energy Systems 28, 416–428.

Harcourt, F., Angeloudis, A., Piggott, M.D., 2019. Utilising the flexible generation potential of tidal range power plants to optimise economic value. Applied Energy 237, 873 – 884. URL: http://www.sciencedirect.com/science/article/pii/S0306261918319093, doi:https://doi.org/10.1016/j.apenergy.2018.12.091.

Kärnä, T., De Brye, B., Gourgue, O., Lambrechts, J., Comblen, R., Legat, V., Deleersnijder, E., 2011. A fully implicit wetting–drying method for dg-fem shallow water models, with an application to the scheldt estuary. Computer Methods in Applied Mechanics and Engineering 200, 509–524.

Kärnä, T., Kramer, S.C., Mitchell, L., Ham, D.A., Piggott, M.D., Baptista, A.M., 2018. Thetis coastal ocean model: discontinuous galerkin discretization for the three-dimensional hydrostatic equations. Geoscientific Model Development 11, 4359–4382. URL: https://gmd.copernicus.org/articles/11/4359/2018/, doi:10.5194/gmd-11-4359-2018.

Kim, G., Lee, M.E., Lee, K.S., Park, J.S., Jeong, W.M., Kang, S.K., Soh, J.G., Kim, H., 2012. An overview of ocean renewable energy resources in korea. Renewable and Sustainable Energy Reviews 16, 2278–2288.

Kramer, S.C., Piggott, M.D., 2016. A correction to the enhanced bottom drag parameterisation of tidal turbines. Renewable Energy 92, 385 – 396. URL: http://www.sciencedirect.com/science/article/pii/S0960148116301239, doi:https://doi.org/10.1016/j.renene.2016.02.022.

Martin-Short, R., Hill, J., Kramer, S., Avdis, A., Allison, P., Piggott, M., 2015. Tidal resource extraction in the Pentland Firth, UK: Potential impacts on flow regime and sediment transport in the Inner Sound of Stroma. Renewable Energy 76, 596–607.

Mitusch, S.K., Funke, S.W., Dokken, J.S., 2019. dolfin-adjoint 2018.1: automated adjoints for fenics and firedrake. Journal of Open Source Software 4, 1292. URL: https://doi.org/10.21105/joss.01292, doi:10.21105/joss.01292.

Moore, T., Boyle, C., 2014. The tidal energy potential of the manukau harbour, new zealand. Sustainable Energy Technologies and Assessments 8, 66–73.

O'Doherty, D.M., Mason-Jones, A., Morris, C., O'Doherty, T., Byrne, C., Prickett, P.W., Grosvenor, R.I., et al., 2011. Interaction of marine turbines in close proximity, in: 9th European Wave and Tidal Energy Conference (EWTEC). Southampton, UK, pp. 10–14.

Schwedes, T., Ham, D.A., Funke, S.W., Piggott, M.D., 2017. Mesh dependence in pde-constrained optimisation, in: Mesh Dependence in PDE-Constrained Optimisation. Springer, pp. 53–78.

Vouriot, C.V.M., Angeloudis, A., Kramer, S.C., Piggott, M.D., 2019. Fate of large-scale vortices in idealized tidal lagoons. Environmental Fluid Mechanics 19, 329–348. URL: https://doi.org/10.1007/s10652-018-9626-4, doi:10.1007/s10652-018-9626-4.

Wang, S., Yuan, P., Li, D., Jiao, Y., 2011. An overview of ocean renewable energy in china. Renewable and Sustainable Energy Reviews 15, 91–111.

Wang, Y., Zhai, Y., Zhang, J., Tong, L., Song, S., Zhang, T., 2017. Numerical study on layout optimization of tidal stream turbines in zhoushan demonstration project, in: The 9th International Conference on Asia and Pacific Coasts 2017, World Scientific. pp. 278–283.

Wang, Z.F., Zhou, L.M., ZHNAG, G.B., WANG, A.F., 2010. Tidal stream energy assessment in specific channels of zhoushan sea area. Periodical of Ocean University of China 8.

Wessel, P., Smith, W.H., 1996. A global, self-consistent, hierarchical, high-resolution shoreline database. Journal of Geophysical Research: Solid Earth 101, 8741–8743.

Zhang, C., Zhang, J., Tong, L., Guo, Y., Zhang, P., 2020a. Investigation of array layout of tidal stream turbines on energy extraction efficiency. Ocean Engineering 196, 106775.

Zhang, J., Cao, Y., Wu, X., Song, F., Dai, P., 2017. Investigation of hydrodynamic characteristics around parallel-arranged horizontal-axis tidal stream turbines. Journal of Hohai University (natural science) 45, 256–262.

Zhang, J., Lin, X., Wang, R., Guo, Y., Zhang, C., Zhang, Y., 2020b. Flow structures in wake of a pile-supported horizontal axis tidal stream turbine. Renewable Energy 147, 2321–2334.

Zhang, Y., Zhang, J., Lin, X., Wang, R., Zhang, C., Zhao, J., 2020c. Experimental investigation into downstream field of a horizontal axis tidal stream turbine supported by a mono pile. Applied Ocean Research 101, 102257.

Zheng, J., Zhang, J., 2015. Recent advances and key technologies in marine energy utilization engineering. Journal of Hohai University (natural science) , 450–455.